Crystal structure prediction of quasi-two-dimensional lead halide perovskites

Juraj Ovčar,[1] Luca Grisanti,[1,*] Bruno Mladineo,[1] Aleksandra B. Djurišić,[2] Jasminka Popović,[1,†] and Ivor Lončarić[1,‡]
[1]*Ruđer Bošković Institute, Bijenička 54, Zagreb 10000, Croatia*
[2]*Department of Physics, The University of Hong Kong, Pokfulam Road, Hong Kong, Hong Kong SAR, China*

(Received 26 April 2022; revised 11 February 2023; accepted 1 May 2023; published 15 May 2023)

Two-dimensional lead halide perovskites are promising materials for optoelectronics due to the tunability of their properties with the number of lead halide layers and the choice of an organic spacer. Physical understanding for the rational design of materials primarily requires knowledge of crystal structure. Two-dimensional lead halide perovskites are usually prepared in the form of films, complicating the experimental determination of structure. To enable theoretical studies of experimentally unresolvable structures as well as high-throughput virtual screening, we present an algorithm for crystal structure prediction of lead halide perovskites. Using an automatically prepared classical potential we show that our algorithm enables fast access to a structure that can be used for further first-principles studies.

DOI: 10.1103/PhysRevB.107.174109

I. INTRODUCTION

In recent years, metal halide perovskites (MHPs) have proven to be promising candidates for the future materials of choice for manufacturing light-emitting diodes (LEDs) and solar cells [1,2]. A subclass of MHPs of particular interest for LED applications are the quasi-two-dimensional (2D) layered perovskites (Q2DPs) due to larger exciton binding energies, improved stability, and wider tunability of properties compared to three-dimensional (3D) perovskites [3]. Particularly, the Ruddlesden-Popper and Dion-Jacobson MHP phases have gained significant attention [4,5]. The general chemical formula of Ruddlesden-Popper perovskites (RPPs) is $R_2A_{n-1}B_nX_{3n+1}$, where R^+ is a large amine spacer cation, A^+ is a smaller organic cation or Cs^+, B^{2+} is a divalent metal cation, X^- is a halide anion, and n is the number of layers of BX_6 octahedra separated by a bilayer of R^+ spacer cations (3D perovskite ABX_3 is obtained in the limit $n \to \infty$). Similarly, the chemical formula of Dion-Jacobson perovskites (DJPs) is $RA_{n-1}B_nX_{3n+1}$, with the difference compared to RPPs being that R^{2+} is a *diammonium* cation. This generality of composition offers a great variety of possibilities in choosing n as well as the particular chemicals involved in the synthesis of the layered perovskites, allowing for the characteristic wide tunability of the RPP and DJP physical properties [3].

Knowledge of the crystal structure of a material is the starting point for understanding its physical properties. Despite constant advances in methodologies [6–9], crystal structure determination from powder-diffraction data cannot be yet considered a trivial task because the information from 3D reciprocal space collapses into its one-dimensional (1D) projection. Although not as straightforward as the structure solution from single crystals, a huge number of crystalline phases have been successfully solved from the powder-diffraction data over the years [10]. On the other hand, when the sample is prepared in the form of a thin film, as almost always is the case in Q2DP-based LED and/or solar cell research, the determination of structure becomes close to impossible not only due to the strong influence of crystalline texture on the diffracted intensities but also due to the limited and inadequate methodologies. There have been some rare attempts to utilize a grazing incidence X-ray diffraction (GIXRD) with molecular modeling aiming to determine purely organic structures prepared in the form of thin films [11], but, on the practical side, the implementation in everyday laboratory work is restricted due to the requirement that data must be collected using synchrotron radiation. Even if the equipment is readily accessible, due to currently underdeveloped methodology that would properly deal with texture-related issues of thin films, such an approach certainly is not efficient enough to elucidate the immense number of novel Q2DP structures that emerge on a daily basis. Considering the inability to solve the structures from the thin-film diffraction data, one way to deal with unknown structures in Q2DP films would be to prepare them in the form of a single crystal or powders. However, there are experimental difficulties when growing materials in the form of a single crystal [12], for example, due to limitations in the stability. In this scenario, many structures of large technological potential remain unknown.

Moreover, it would be greatly valuable to know the structure even before the materials are synthesized. It is, therefore, desirable to use a computational tool to find, understand, and predict stable Q2DP crystal structures as well as their physical properties. Different computational approaches have been proposed to explore the possibility of formation of various 3D perovskites [13–15]. Similar computational explorations of Q2DPs have been scarce [16,17] and did not aim to find the global minimum energy structure, most likely due to the prohibitively vast compositional phase space and large system sizes.

*luca.grisanti@irb.hr
†jasminka.popovic@irb.hr
‡ivor.loncaric@gmail.com

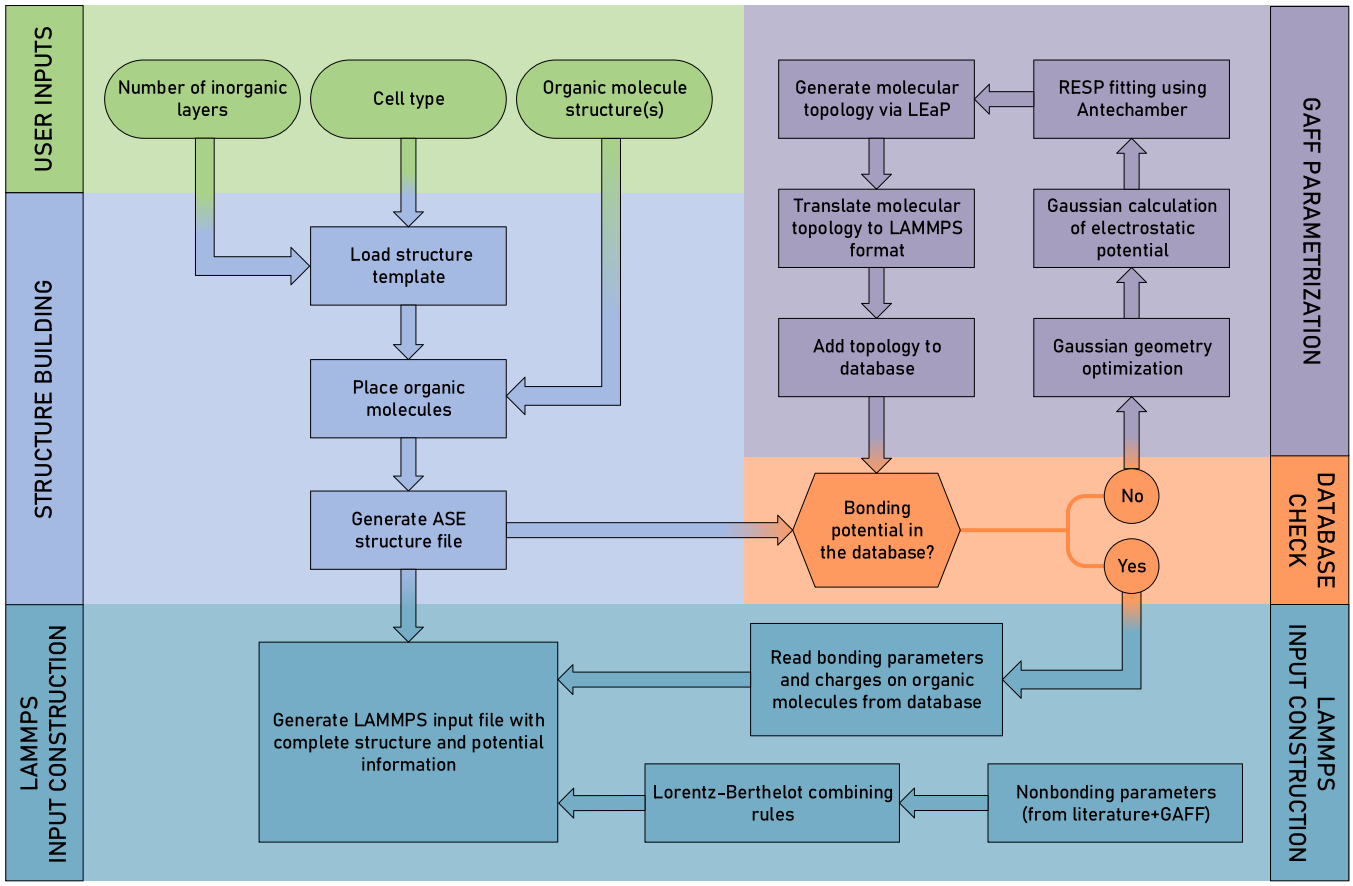

FIG. 1. Flowchart of the procedure of generating an input LAMMPS file containing information on the structure and interatomic interactions of a Q2DP.

Generally, density functional theory (DFT) is utilized abundantly due to its well-known good balance between accuracy and low computational cost. However, in the case of Q2DPs, the approach to crystal structure prediction via DFT suffers from several drawbacks. Optimizing an initial-guess structure using a local structural relaxation algorithm gives no guarantee that the final structure is the global minimum. This may be resolved by exploring a sufficiently large part of the potential energy surface (PES), but this is computationally unfeasible, as in the case where Q2DPs unit cells may contain several hundreds of atoms, giving rise to complex PESs [18].

In this work, we introduce a workflow for predicting candidate Q2DP crystal structures using classical model potentials combined with DFT. The potentials are constructed in an automated fashion and then employed to find a global minimum structure via a minima hopping algorithm in the vein of Goedecker [19], Amsler and Goedecker [20], and Peterson [21]. In this work, we will refer to the developed algorithm as GO-MHALP (global optimization via minima hopping algorithm for layered perovskites). We aim to develop a method which is generalizable, but specialized to work for Q2DP structures with well-defined general structural features, such as the alternating organic/inorganic layered structure. Therefore, we expect to start from structures not too far from a global minimum so that minima hopping is a well-suited technique, as opposed to methods which work well when starting far away from the global minimum, such as particle swarm optimization [22] or genetic algorithms [23]. Our method works in principle for any candidate Q2DP whose R^+/R^{2+} and A^+ compounds are organic cations consisting of N, C, and H and whose inorganic perovskite octahedra are $PbBr_6$. The complete methodology is described in Sec. II while validations of the model on RPPs containing butylammonium (BA) and methylammonium (MA) and a DJP containing 4-(aminomethyl)-piperidinium (4AMP) are presented in Sec. III. Additionally, we have extended the method to predict an unknown Q2DP structure containing mixed-halide perovskite octahedra $PbBr_3I_3$ [24].

II. METHODOLOGY

In the following two sections, we describe the procedure of generating structures and the accompanying classical potentials which are used as inputs for GO-MHALP. A visual aid in the form of a flowchart of the procedure can be viewed in Fig. 1. In the third section, we describe the GO-MHALP algorithm itself with an accompanying flowchart in Fig. 2.

A. Initial structures generation

One of the advantages of structure prediction using global optimization algorithms is that the final set of found structures should not depend strongly on the starting structure inputted

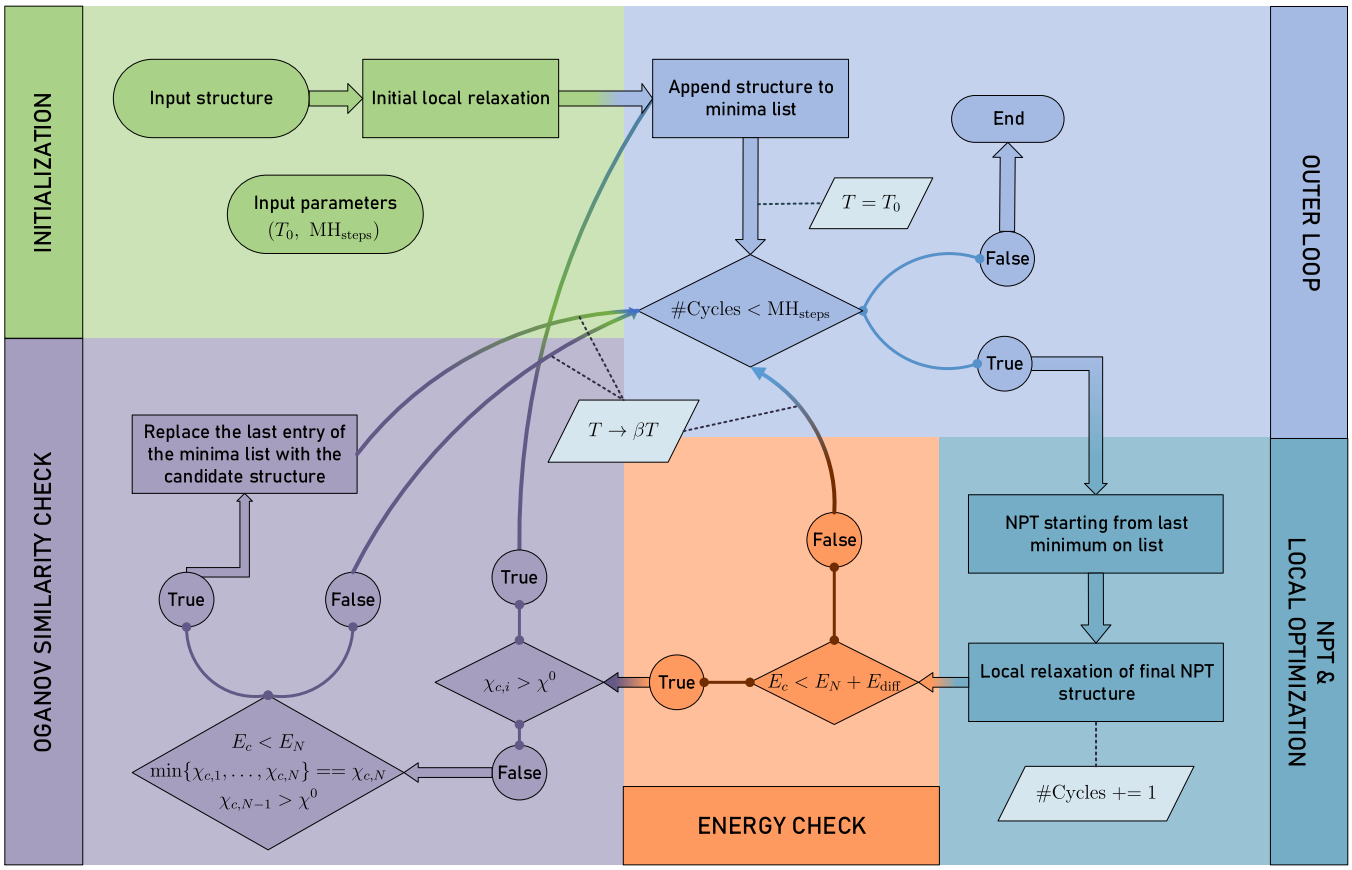

FIG. 2. Flowchart of the full GO-MHALP algorithm. Dashed lines indicate parameter changes at certain steps.

to the algorithm. However, in the particular case of minima hopping, it is necessary to start from a region in configuration space for which the potential has a physical meaning, i.e., in our case, the starting structure should resemble a Q2DP. To this end, we developed an automatized procedure for the generation of idealized Q2DP structures for a given R molecule.

We investigated three types of initially tetragonal cell geometries with parallel or offset interlayer configurations, making a total of six different types of input structures as shown in Fig. 3. These cell types were chosen because known Q2DP structures often form these geometries [25]. Furthermore, in the various cell types, the supercells can be rearranged to produce equivalent structures, providing an additional check of the independence of the found global minimum on the initial guess structure. The parallel and offset structures are related by a layer shift, while the 1×1 and $\sqrt{2} \times \sqrt{2}$ are subcells of the 2×2 cell type.

We prepared multiple template structures by arranging the inorganic layers in ideal aforementioned configurations and (for $n > 1$) placing MA molecules at the centers of inorganic cages. The R^+/R^{2+} organic cations are first added to the template structures so that the NH_3 groups of the cations are placed approximately at the centers of the inorganic pockets. For RPPs, the cations are reoriented in such a way so that the vector from the N atom towards the respective cation's center of mass points in a predefined direction towards the neighboring inorganic sheet. The interlayer spacing between the inorganic sheets can be adjusted as needed to accommodate spacers of various lengths. We advise the reader to see the code in Ref. [26] as well as Sec. 3 in the Supplemental Material [27] for further details. All generated initial guess structures are given in the Supplemental Material in CIF format as well.

Since we are ultimately interested in global structure optimizations in which the starting structure should not be of decisive importance, this simple way of generating structures works very well for our intentions since it is automatic and fast.

B. Construction of classical potentials

Following previous work [28–32], and in particular the idea behind the methylammonium lead halide (MAPI) family of potentials developed by Mattoni *et al.* [30,31], we undertake an approach where the total classical potential is modeled as a sum of (i) nonbonding potential that depends only on the interatomic distances with only two-body terms taken into account and (ii) a bonding potential including bonds, dihedrals, and angles as described by general Amber force field (GAFF) [33], a generalization of the assisted model building with energy refinement (AMBER) [34] force field.

Denoting the list of positions of the nuclei with $\{\boldsymbol{R}\} \coloneqq (\boldsymbol{R}_1, \boldsymbol{R}_2, \ldots, \boldsymbol{R}_N)$, the general form of the total potential energy can be written as

$$U(\{\boldsymbol{R}\}) = \frac{1}{2}\sum_{i,j}^{N} U_{ij}(R_{ij}) + U^{\mathrm{bonding}}, \tag{1}$$

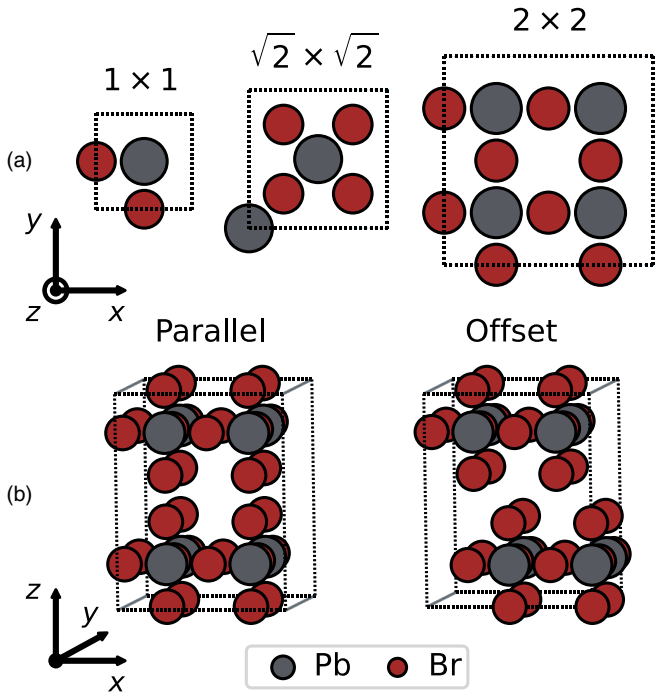

FIG. 3. Types of initial cell configurations. (a) Cross sections perpendicular to the long cell axis with the cell dimensions labeled in units of Pb-Pb distance $d_{\text{Pb-Pb}} = 6.080$ Å. (b) Interlayer configurations shown for the 2×2 cell type. The long cell axis is shortened and organic molecules are removed for clarity. In the offset configuration the layers are shifted by a quarter of the unit cell length in the x and y directions.

where $R_{ij} := |\boldsymbol{R}_i - \boldsymbol{R}_j|$. As in all effective-potential approaches, the electronic degrees of freedom do not enter the calculation explicitly but are rather absorbed into the effective interactions of the nuclei [35].

U_{ij} is separated into three parts, dealing with the nonbonding inorganic-inorganic (II), inorganic-organic (IO), and organic-organic (OO) interatomic interactions, respectively:

$$U_{ij} = U_{ij}^{\text{II}} + U_{ij}^{\text{IO}} + U_{ij}^{\text{OO}}. \tag{2}$$

The explicit form of the inorganic-inorganic interaction is

$$U_{ij}^{\text{II}}(R_{ij}) = A_{ij}\exp(-R_{ij}/\rho_{ij}) - \frac{c_{ij}}{R_{ij}^6} + \frac{q_i q_j}{4\pi\epsilon_0 R_{ij}}, \tag{3}$$

where the first two terms comprise the Buckingham potential [36] with the first term describing the Pauli repulsion at small nuclei distance and the second term describing the van der Waals interaction with A_{ij}, ρ_{ij}, and c_{ij} as model parameters. The final term is the Coulomb interaction between two (possibly partial) ionic charges. This choice of the form of the inorganic-inorganic interaction follows the approach originally undertaken by Matsui *et al.* [28] to model $MgSiO_3$ ilmenite and $MgSiO_3$ perovskite. This simplified approach regards the interactions within the inorganic layer as prevalently ionic and cannot fully describe the covalent effects of lead-halide interactions present in hybrid lead halide perovskites [37–39]. Nonetheless, we choose this simplification for the sake of the transferability of the potential. The limitations of the Buckingham-Coulomb potential in describing lead-halide interactions and more complex models which could possibly resolve these shortcomings are discussed by Mattoni, Filippetti, and Caddeo [40]. The inorganic-organic interaction is modeled as follows:

$$U_{ij}^{\text{IO}}(R_{ij}) = A_{ij}\exp(-R_{ij}/\rho_{ij}) - \frac{c_{ij}}{R_{ij}^6} + \frac{q_i q_j}{4\pi\epsilon_0 R_{ij}} + 4\epsilon_{ij}\left[-\left(\frac{\sigma_{ij}}{R_{ij}}\right)^6 + \left(\frac{\sigma_{ij}}{R_{ij}}\right)^{12}\right], \tag{4}$$

i.e., besides the Buckingham and Coulomb terms a Lennard-Jones term is added with additional parameters ϵ_{ij} and σ_{ij}. For (Pb, Br)-(C, N) interactions only the Buckingham and Coulomb terms are used, while only Coulomb and Lennard-Jones terms are used for (Pb, Br)-H interactions. This form of the inorganic-organic interactions is appropriate due to the fact that the inorganic (Pb, halide) and organic orbitals are electronically separated [40]. Similarly, nonbonding organic-organic interactions are described only by Lennard-Jones and Coulomb terms:

$$U_{ij}^{\text{OO}}(R_{ij}) = 4\epsilon_{ij}\left[-\left(\frac{\sigma_{ij}}{R_{ij}}\right)^6 + \left(\frac{\sigma_{ij}}{R_{ij}}\right)^{12}\right] + \frac{q_i q_j}{4\pi\epsilon_0 R_{ij}}. \tag{5}$$

For U_{ij}^{II}, U_{ij}^{IO}, and U_{ij}^{OO} a cutoff parameter r_c is used so that for $R_{ij} > r_c$ only the long-range Coulomb interaction is calculated using the P^3M algorithm [41]. The bonding potential, which, of course, concerns only interactions within organic molecules, has the following form:

$$U^{\text{bonding}} = \sum_{ij}^{N} K_{ij}^{\text{b}}\left(R_{ij} - R_{ij}^0\right)^2 + \sum_{ijk}^{N} K_{ijk}^{\text{a}}\left(\theta_{ijk} - \theta_{ijk}^0\right)^2 + \sum_{ijkl}^{N} K_{ijkl}^{\text{d}}\left(1 + \cos\left(n_{ijkl}\phi_{ijkl} - \phi_{ijkl}^0\right)\right), \tag{6}$$

expressing bonds, angles, and dihedrals, respectively. R_{ij} are two-body distances, θ_{ijk} are three-body angles, and ϕ_{ijkl} are four-body dihedrals while the other factors are GAFF parameters. The main advantage of the GAFF force field is its capability to describe a very large number of organic molecules with an acceptable level of accuracy. Besides, its standard working frame allows in principle an automatic atom type assignment for any given organic molecule in its (reliably) relaxed geometry.

The idea of GO-MHALP is to have a general and flexible tool that can be applied to any organic molecule R in a candidate Q2DP structure. If the particular molecule is not found in the local database of organic cations the potential can be generated in the very first step provided a starting geometry along with the GAFF philosophy. Shortly, to obtain GAFF parameters the geometry of the R^+ molecule is optimized using the Gaussian [42] program with the B3LYP [43–46] hybrid DFT functional and 6-311G* basis set [47–49]. Consistently with previous work [30], the electrostatic potential (ESP) of the optimized isolated cation with +1 total charge is obtained via the BP86 [43,50–52] generalized gradient approximation (GGA) functional and the Def2TZVP [53,54] basis set. Partial atomic charges are then obtained by directly fitting this *ab initio* ESP using the restrained electrostatic potential (RESP)

[55] method as implemented in the Antechamber [56] program from the Amber16 suite [57,58]. Complete molecular topology and GAFF parameters are generated and translated to LAMMPS [59] format and added to the local database of organic cations.

The parameters for the C-C, N-N, and H-H nonbonding Lennard-Jones interactions are obtained from GAFF parametrization as described above. As for the nonbonding parameters concerning Pb-Pb and Br-Br interactions, the values of these are taken to be the same as the ones obtained by Hata *et al.* [31] for $MAPbBr_3$, barring the charges q_i, which for organic molecules we set to the partial charges obtained by RESP fitting and for the atoms comprising the inorganic perovskite structure we set $q_{\mathrm{Pb}} = +2$ and $q_{\mathrm{Br}} = -1$. The reason for this is that the charges from Hata *et al.* were set by rescaling of charges obtained by Mattoni *et al.* [30] for $MAPbI_3$ and in both of these works the obtained charges of the inorganic lattice $PbBr_3$ do not sum up to 1. In Ref. [30] system neutrality was then ensured by refitting the charge parameters of the whole model (including MA) to data obtained via DFT. The main physical shortcoming of setting integer charges is the loss of the ability to describe a part of the covalency effects in the lead-halide interactions [28]. However, for this work, by setting integer charges we avoid the need for expensive DFT calculations and refitting procedures, thus greatly increasing the transferability of this method for construction of classical potentials.

A benchmark of the accuracy of the potentials may be found in the Supplemental Material [27].

C. Minima hopping

Minima hopping (MH) is an efficient and simple global optimization method first developed by Goedecker [19]. The general idea is to alternate between molecular dynamics (MD) simulations and local structure optimizations (relaxations) after which some criteria are used to determine whether the optimized structure will be accepted as a newfound local minimum. A system may gain enough kinetic energy during MD to overcome a potential barrier and, in this way, a complex PES may be traversed to arrive at different potential energy basins.

The original MH method conceived by Goedecker concerned only nonperiodic systems and therefore employed only local optimizations of atomic positions. However, the ground state of a crystalline system is fully determined not only by atomic positions but also by the unit cell parameters. Therefore, by using variable cell shape MD, Amsler and Goedecker generalized the MH method to be functional for periodic systems as well [20]. Another variant of MH, dubbed constrained minima hopping, was developed by Peterson [21]. Peterson introduced a simple constraint, based on Hooke's law, in order to prevent dissociation of molecules adsorbed on a surface during the MD portion of MH, thereby effectively reducing the configurational space to be explored by MH only to configurations of interest (namely, those where the adsorbate identity is preserved).

In this work, we combine and modify the approaches introduced above to develop an MH algorithm suitable for Q2DP global structure optimization: GO-MHALP. We simulate MD in the isothermal-isobaric (*NPT*) ensemble and optimize the unit cell as well as atomic positions during local optimizations. Additionally, we developed a scheme for detailed exploration of local energy basins and on-the-fly selection of the lowest energy structures found in them.

We implemented our algorithm based on an MH algorithm already existing within the ASE [60] package using the LAMMPSlib interface to read in the classical potential described in Sec. II B. Now we present an outline of the algorithm. A list of initial parameters and their descriptions and values can found in Table I.

The input structure is fed into the algorithm and its cell and atomic positions are optimized. This optimized structure is the first entry in the list of found local minima. The initial optimization is performed with a looser force convergence threshold than following optimizations to avoid a long optimization step since the initial structure may be far away from a local minimum. For ease of writing, from now on we will label the physical properties of the entries in the list of found local minima with the subscript i, where $i = 1, \ldots, N$ so that N labels the last found minimum. At this point, there is only one structure in the list of found minima, i.e., $N = 1$.

An *NPT* [61–63] molecular dynamics simulation is performed starting from the locally optimized structure at temperature $T = T_0$ and with other parameter values being as listed in Table I. The values of the *NPT* related parameters were chosen to ensure that the molecular dynamics is long enough for the system to completely thermalize. Generally, the starting *NPT* configuration is the last (Nth) minimum in the list of found minima and T varies during GO-MHALP as described below. Ions are given random initial velocities corresponding to a Maxwell-Boltzmann distribution of temperature T. *NPT* is stopped after $\mathrm{md}_{\mathrm{min}}$ local minima have been passed over with one pass counted if a sequence of potential energies calculated at each MD step ends with two downward points followed by two upward points.

The atomic positions and cell parameters of the last configuration obtained by *NPT* dynamics are optimized. We label the physical properties of this candidate structure with the subscript c. After optimization, energy and structure similarity checks are performed to determine whether the candidate structure will be added to the list of local minima. First, E_c is compared to E_N; if $E_c > E_N + E_{\mathrm{diff}}$, the structure is discarded as being too high in energy, *NPT* temperature is increased, i.e., $T \to \beta T$, and a new *NPT* or optimization cycle is started from the Nth minimum in the list of found minima. Otherwise, a structure similarity check is performed. For structure comparison we use Oganov fingerprints [64,65], which were first used in the context of MH by Amsler and Goedecker [20]. With this method, for every structure a unique "fingerprint" may be calculated and represented as a matrix in an abstract vector space. The components of the matrix are sums of Gaussian-smeared δ functions:

$$F_{AB}(R) = \sum_{A_k, B_l} \frac{\delta(R - R_{kl})}{4\pi R_{kl}^2 \frac{N_A N_B}{V} \Delta} - 1, \tag{7}$$

where the sum runs over all pairs of atoms of types A and B found within the cutoff distance $R_{kl} < R_c$, with N_A and N_B being the number of atoms of the respective type A and B in the unit cell and V being the unit cell volume. Each fingerprint

TABLE I. List of parameters used in the MH algorithm.

Outer loop	Value	Description
MH_{steps}	170	Algorithm stops after completing MH_{steps} minima hopping cycles
md_{min}	4000	Number of local minima to be passed through before stopping *NPT* dynamics
T_0 (K)	50	Initial temperature of *NPT* dynamics; temperature is reset to T_0 if a minimum is accepted
β	1.1	Factor by which the temperature of the *NPT* thermostat is multiplied if a candidate minimum is rejected
E_{diff} (eV)	1.1	If a candidate structure is greater in energy compared to the last found minimum by E_{diff}, the candidate is rejected
NPT		
Δt (fs)	0.5	Time step of *NPT* dynamics
P_0 (eVÅ^{-3})	0.0	Pressure exerted on the system during *NPT* dynamics
τ (fs)	25.0	Characteristic timescale of the thermostat
W (eVfs^{2}Å^{-3})	337.5	A constant in the barostat differential equation
Local optimizations		
Optimizer	BFGS	The local optimization algorithm
F_{init} (eV Å^{-1})	0.05	Total force convergence threshold for the initial cell optimization
F_{geo} (eV Å^{-1})	0.1	Total force convergence threshold for geometry optimizations
F_{cell} (eV Å^{-1})	0.01	Total force convergence threshold for cell optimizations
Oganov fingerprints		
χ^0	0.005	Maximum cosine distance between two structures below which they are considered to be the same structure
Δ (Å)	0.05	Width of the bins into which the Oganov fingerprint components are discretized
σ (Å)	0.1	Standard deviation of the Gaussian smearing of fingerprints
N_σ	5	Number of standard deviations σ at which the Gaussian smearing is cut off
R_c (Å)	l_{min}	Cutoff radius in angstrom for the fingerprints. At every MH step, the shortest cell length l_{min} is used

component $F_{AB}(R)$ is discretized into bins of width Δ so it can be represented as a vector with the mth vector coordinate being the value of the fingerprint component $F_{AB}(m)$. A *cosine distance* $\chi_{i,j}$ may then be defined as a measure of dissimilarity of structures i and j:

$$\chi_{i,j} = \frac{1}{2}\left(1 - \frac{\sum_{AB}\sum_m F^i_{AB}(m)F^j_{AB}(m)w_{AB}}{\sqrt{W^i W^j}}\right), \tag{8}$$

where the importance weight w_{AB} is defined as

$$w_{AB} = \frac{N_A N_B}{\sum_{\text{cell}} N_A N_B} \tag{9}$$

and W^i is the norm

$$W^i = \sum_{AB}\sum_m \left[F^i_{AB}(m)\right]^2 w_{AB}. \tag{10}$$

To reduce noise, we excluded hydrogen atoms from the calculation of cosine distances. The cosine distance $\chi_{c,i}$ is calculated as a measure of dissimilarity between the candidate structure and a structure i from the list of found local minima. If $\chi_{c,i} > \chi^0$ for every i and the threshold parameter χ^0, the candidate structure is added to the local minima list and the *NPT* temperature is reset to the initial temperature T_0. Otherwise, the candidate structure is considered not to be a unique minimum and the *NPT* temperature is increased, i.e., $T \to \beta T$. The candidate structure replaces the Nth minimum if the following three conditions are met: $E_c < E_N$, $\min\{\chi_{c,1}, \ldots, \chi_{c,N}\} = \chi_{c,N}$, and $\chi_{c,N-1} > \chi^0$. With this replacement scheme and the choice of parameters as listed in Table I, we found that the algorithm correctly explores local potential energy basins while preserving structural dissimilarity of the found minima.

This concludes a complete MH cycle in our GO-MHALP frame. If the number of cycles is less than the given MH_{steps} parameter the algorithm will start a new *NPT* simulation from the last found minimum and otherwise the algorithm stops.

D. DFT calculations

On specific structures (see below), DFT relaxations were additionally performed in order to validate and refine the results. All DFT relaxations were performed using the plane-wave basis set code QUANTUM ESPRESSO [66,67] with the plane-wave basis set cutoff being 816 eV. Garrity-Bennet-Rabe-Vanderbilt (GBRV) pseudopotentials [68] were employed together with the vdW-DF-cx exchange-correlation functional [69]. A Monkhorst-Pack k-point mesh [70] with a density of 5 Å was used for Brillouin zone integration. The atomic positions and the unit cell parameters were relaxed until the pressure, the forces on each atom, and the total energy change were smaller than 0.5 kbar, 0.02 eV Å^{-1}, and 1 meV, respectively.

E. Similarity measures of simulated powder XRD patterns

In order to assess the validity of the predicted structures with our protocol, we quantified the similarity of structures obtained with GO-MHALP to structures solved from single-crystal X-ray diffraction (XRD) data by simulating their powder XRD (PXRD) patterns and calculating a similarity measure based on cross-correlation functions [71,72] as im-

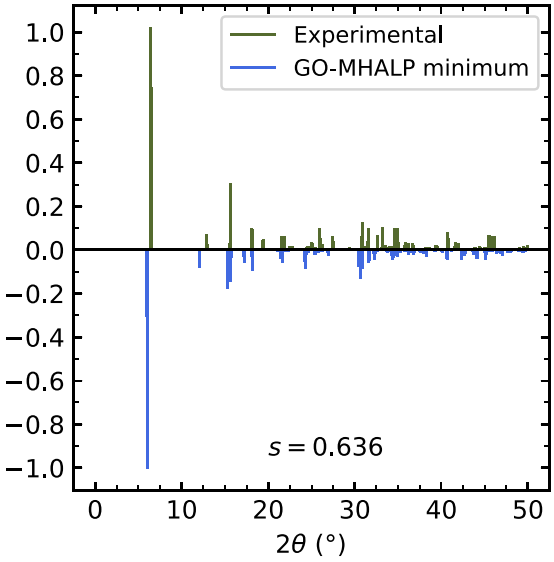

FIG. 4. Comparison of simulated PXRDs of experimentally solved and one of the structures predicted with GO-MHALP of BA_2PbBr_4. PXRD intensity is scaled so that the highest peak has the value 1.0. In this example the similarity measure amounts to $s = 0.636$.

plemented in the PyXtal [73] PYTHON library. Explicitly, the similarity measure s_{12} of two powder diagrams $y_1(\theta)$ and $y_2(\theta)$, invariant against scaling of the PXRD intensities, is calculated as

$$s_{12} = \frac{\int w(r)c_{12}(r)dr}{\left[\int w(r)c_{11}dr \int w(r)c_{22}(r)dr\right]^{1/2}}, \tag{11}$$

where c_{12} is the cross-correlation function,

$$c_{12}(r) = \int y_1(\theta)y_2(\theta + r)d\theta, \tag{12}$$

with the autocorrelation functions c_{11} and c_{22} defined analogously. We used the cosine weighting function

$$w(r) = \begin{cases} 0.5\left(\cos\left(\pi \frac{r}{l}\right) + 1\right), & |r| < l \\ 0, & |r| > l \end{cases} \tag{13}$$

with the cutoff $l = 1.0°$. The similarity measure adopts values between 0 and 1, where $s_{12} = 1$ corresponds to identical PXRDs. An example of a comparison of PXRDs simulated from an experimentally solved structure and a minimum obtained with GO-MHALP is shown in Fig. 4.

F. Potentials for iodine and mixed-halide systems

GO-MHALP is a general procedure which can in principle, given a suitable classical potential, be used for any systems. For example, classical potentials for Q2DPs containing iodine instead of bromide can be constructed in a completely analogous manner as described in Sec. II B, but using the parameters for $MAPbI_3$ [30,32]. As detailed in an another work [24], we employed GO-MHALP to predict a mixed-halide structure. We use the Berthelot rule to calculate the Buckingham parameters for Pb-Pb and Br-I interactions:

$$A^{\text{mixed}} = \sqrt{A^{\text{Br}}A^{\text{I}}}, \tag{14}$$

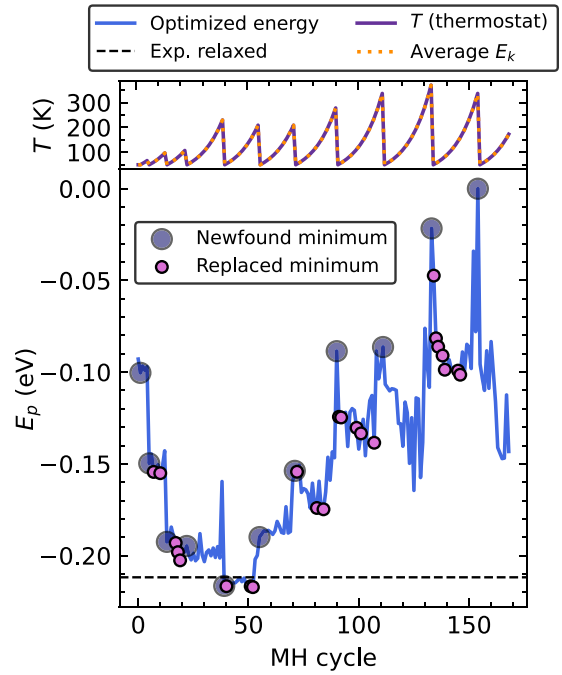

FIG. 5. Summary of a GO-MHALP run for BA_2PbBr_4 with the 2×2 cell type and initially offset layers. Top: *NPT* thermostat temperature and the average kinetic energy of the last 20 ps of MD across MH cycles. Bottom: Classical potential energies of the candidate structures across the run (blue) and the experimentally solved structure relaxed with the classical potential (dashed black). Identified local minima are marked with circles.

where A^{Br} and A^{I} denote Buckingham parameters used for pure halide structures and A^{mixed} are Buckingham parameters used for the mixed-halide structures.

III. RESULTS AND DISCUSSION

We first validate GO-MHALP on the well-known case of $R^+ = BA^+$ (butylammonium) cation as spacer. Both BA_2PbBr_4 and $BA_2MAPb_2Br_7$ have been successfully prepared and their crystal structures were solved [74,75]. Following the tests on RPPs with BA we continue the validation of GO-MHALP on a DJP structure containing 4-(aminomethyl)-piperidinium (4AMP) [3]. We use the experimentally obtained structures as reference points for validation of GO-MHALP predictions. Radial distribution functions and simulated PXRD patterns for relevant (predicted and experimental) structures may be found in the Supplemental Material [27], as well as the CIF files of these structures.

Finally, we show performance of GO-MHALP to predict a structure of a mixed-halide Q2DP *t*-$BA_2PbBr_2I_2$. This structure was experimentally solved after the prediction with GO-MHALP.

A. BA_2PbBr_4

We first applied GO-MHALP to BA_2PbBr_4 RPP. The six types of unit cells described in Sec. II A were used as inputs. A summary of a GO-MHALP run is shown in Fig. 5. First, the top panel shows that during MD the system is well thermalized to the set thermostat temperature. Potential energy

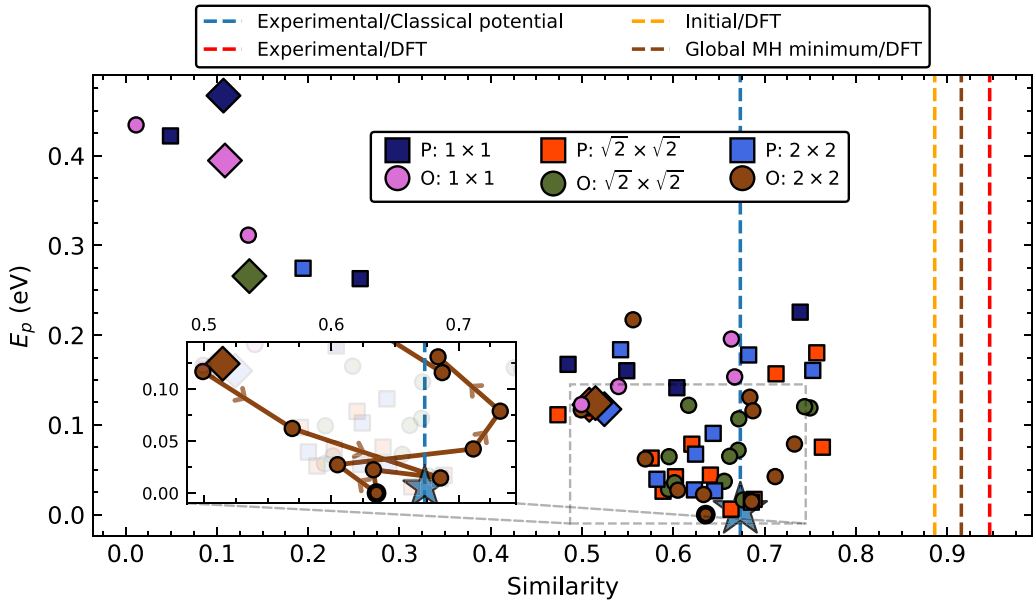

FIG. 6. Similarity measures and potential energies of minima obtained with GO-MHALP for BA_2PbBr_4. The vertical dashed lines labeled in legend as X/Y show similarity measures of structures X relaxed with Y level of theory (see text). Different markers indicate different cell types, where P (O) indicates an initially parallel (offset) structure (see Sec. II A). Diamonds (♦) indicate the starting GO-MHALP points after initial relaxation. The star (★) indicates the similarity measure and energy of the experimental structure relaxed with the classical potential. The order of the accepted minima for the optimal cell type is shown in the inset with the global GO-MHALP minimum emphasized with a bolded edge. Energies are shown per formula unit with the zero of the potential energy chosen as the energy of the global GO-MHALP minimum.

barriers are overcome by gradually increasing the temperature and newfound minima are accepted upon entrance into a local energy basin. After each restart of the *NPT* temperature to T_0, GO-MHALP explores the surrounding configuration space in detail and the replacement scheme described in Sec. II C selects the lowest energy structure found in a basin. The global minimum for this run, i.e., the lowest energy local minimum, is found in a distinct basin that lies very close in energy to the experimentally solved structure whose atomic positions and cell parameters were optimized with the classical potential (dashed line). This is an indication that the global minimum of the model potential is connected to the true (experimental) global minimum by a local optimization, a point to which we will return below.

For a complete test and validation of GO-MHALP, we calculated similarity measures of PXRDs between the experimental structure and (a) each of the final minima predicted with six GO-MHALP runs for the six different cell types; (b) experimental structure, relaxed with the classical potential; (c) experimental structure, relaxed with DFT; (d) lowest energy (global) minimum found with GO-MHALP, relaxed with DFT; and (e) the GO-MHALP initial structure from which the global minimum was found, relaxed with DFT.

Similarity measures (a) and (b) are plotted against classical potential energies in Fig. 6 as scatter points and similarity measures (b)–(e) are plotted as vertical dashed lines. In particular, the line corresponding to case (b) sets the practical limit of the similarity measure that can be reached by this version of GO-MHALP.

First of all, we can notice that the energies of the best (lowest energy) minima of 1×1 cell types are noticeably higher than the larger cell types, meaning that GO-MHALP predicts that 1×1 unit cells are too small to capture all experimentally realized degrees of freedom, which is indeed correct as the experimental structure is of the $\sqrt{2} \times \sqrt{2}$ type. The best minima of $\sqrt{2} \times \sqrt{2}$ and 2×2 cell types cluster near the experimental structure relaxed with the classical potential (marked with a star) regardless of the initially parallel or offset interlayers, showing that in these cases GO-MHALP reliably finds the global minimum of the potential regardless of the details of the input structures. While GO-MHALP finds the experimental structure relaxed with the classical potential, agreement of these structures with the true experimental structure is not completely satisfactory (similarity of around 0.7). On the other hand, relaxing the experimental structure with DFT achieves a similarity of 0.95. Clearly, GO-MHALP has the ability to find the global minimum, but the model potential should be improved.

The global minimum itself is found for the initially O: 2×2 cell type, with the best P: 2×2 and the $\sqrt{2} \times \sqrt{2}$ minima being slightly higher in energy. The O: 2×2 input structure after initial relaxation shows already a good similarity of 0.515 which is further improved by GO-MHALP to score 0.635 at the global minimum. Relaxing the global minimum with DFT significantly improves this value to a similarity measure of 0.915. This final step suggests that an extra DFT relaxation of the global minimum found by GO-MHALP renders final structures that can be highly accurate. The small inset in Fig. 6 depicts how the PES exploration works in GO-MHALP in the case of the O: $\sqrt{2} \times \sqrt{2}$ unit cell. The system goes through a couple of minima before locating the basin containing the global minimum.

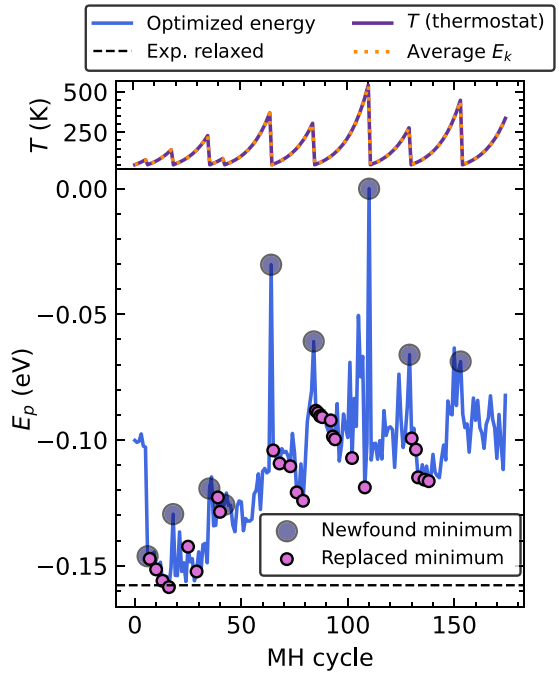

FIG. 7. Summary of a GO-MHALP run for $BA_2MAPb_2Br_7$ with the $\sqrt{2} \times \sqrt{2}$ cell type and initially parallel interlayer configuration. Top: *NPT* thermostat temperature and the average kinetic energy of the last 20 ps of MD across MH cycles. Bottom: Classical potential energies of the candidate structures across the run (blue) and the experimentally solved structure relaxed with the classical potential (dashed black). Identified local minima are marked with circles.

B. $BA_2MAPb_2Br_7$

We continue the validation of GO-MHALP on a similar $n = 2$ RPP: $BA_2MAPb_2Br_7$. The obtained similarity measures are summarized in Fig. S10 [27]. As is the case for BA_2PbBr_4, the global minimum of the potential is near the experimental structure relaxed with the classical potential with a higher similarity measure compared to the $n = 1$ case. A possible rationalization of this fact is that the accuracy of the potential is expected to grow with the number of layers, n, as the potential is constructed using parameters for a 3D perovskite.

GO-MHALP correctly predicts that $BA_2MAPb_2Br_7$ crystallizes in the $\sqrt{2} \times \sqrt{2}$ cell type. The low-energy region of the PES is not as rich as is the case for BA_2PbBr_4 and is surrounded by higher potential barriers. This can be seen in Fig. 7: the first local basin that GO-MHALP found was the one containing the global minimum and higher *NPT* temperatures were needed to overcome basin barriers. The relative flatness of the PES going from the input to the global minimum is the reason why relaxations of input structures, both by using DFT and classical potentials, resulted in structures near the global minimum with an already large similarity measure. Relaxing the found global minimum with DFT again achieves a slightly better similarity (0.940) compared to relaxing the initial structure with DFT (0.930).

C. $(4AMP)PbBr_4$

To validate the GO-MHALP workflow on a Q2DP containing a different spacer, we select the Dion-Jacobson-type perovskite $(4AMP)PbBr_4$ [76]. The 1-(4-piperidinyl)methanamine (4AMP) structure is shown in Fig. 8. At one molecular end, one nitrogen atom belongs to the aminomethyl unit, while the other is within the piperidinyl ring on the opposite side. In a Dion-Jacobson perovskite, these two nitrogens connect to the inorganic perovskite layers. Therefore, neighboring organic 4AMP molecules may differently connect to the same layer; i.e., one 4AMP may connect via the aminomethyl unit and its neighbor via the piperidinium unit. To account for this possibility, we considered the following initial configurations: non-alternating (na), i.e., all neighboring 4AMP molecules connect to a perovskite layer in the same manner; all-alternating (a1), i.e., all neighboring 4AMP molecules connect to a perovskite layer in the opposite manner; and half-alternating (a2), i.e., two neighboring 4AMP molecules connect to a perovskite layer in the same manner, while the other two connect in the opposite manner. Note that configuration (a1) is possible for $\sqrt{2} \times \sqrt{2}$ and 2×2 cell types, while (a2) is possible only for 2×2. It is necessary to explicitly include all these configurations in the initial structures since it is extremely unlikely for the molecules to completely reorient during MD. This gives a total number of 12 types of initial structures for GO-MHALP.

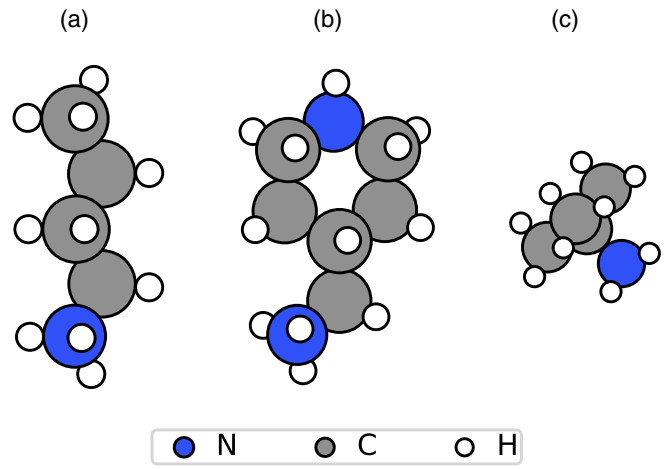

FIG. 8. Organic spacers for which the Q2DP structure was predicted with GO-MHALP: (a) butylammonium (BA), (b) 4-(aminomethyl)-piperidinium (4AMP), and (c) *tert*-butylammonium (*t*-BA).

A summary of a GO-MHALP run is shown in Fig. 9. After locating ten Q2DP local minima (including the minimum obtained with initial relaxation), GO-MHALP is unable to find a new unique minimum, which results in the MD temperature rising to about 600 K. This high-temperature MD "melts" the inorganic perovskite structure, resulting in the newfound local minimum losing its Q2DP character. We deem these "melted" types of structures unphysical predictions as the classical potential is, by construction, well defined only for Q2DPs and we exclude them from following analysis.

The second point to be noted in Fig. 9 is that the energy of the experimentally solved structure relaxed with the classical potential is significantly lower than any of the structures explored by GO-MHALP. The reason for this is that the exper-

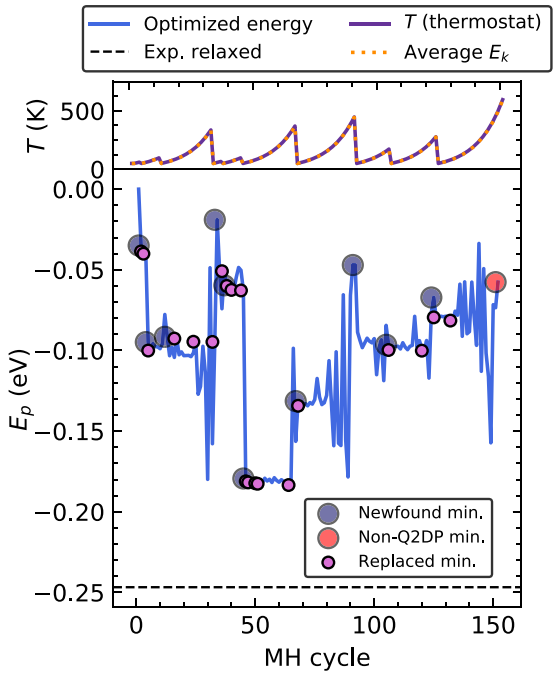

FIG. 9. Summary of a GO-MHALP run for (4AMP)$PbBr_4$ with the $\sqrt{2} \times \sqrt{2}$ cell type, initially parallel interlayer configuration, and alternating 4AMP molecules configuration. Top: *NPT* thermostat temperature and the average kinetic energy of the last 20 ps of MD across MH cycles. Bottom: Classical potential energies of the candidate structures across the run (blue) and the experimentally solved structure relaxed with the classical potential (dashed black). Identified local minima are marked with circles.

imentally resolved structure has more degrees of freedom than the ones describable by configurations in Fig. 9. Specifically, in the notation established in this paper, the experimentally obtained cell is of the $2\sqrt{2} \times \sqrt{2}$ type [76]. This cell type allows for an intricate pattern of alternating 4AMP orientations: along the shorter cell axis, the manner of connection does not change, while it is altered for every *second* neighbor along the long cell axis.

The summary of GO-MHALP runs for all cell types is shown in Fig. S11 [27]. As explained in the last paragraph, all structure types lack the necessary number of degrees of freedom to find the experimental structure relaxed with the classical potential. Relaxing the lowest energy minimum of the O(a2): 2×2 cell type with DFT actually results in worse similarity (0.715) compared to simply relaxing the initial guess structure with DFT (0.776). However, the energy (as calculated with DFT) of the relaxed O(a2): 2×2 minimum is significantly lower than the energy of the relaxed initial guess structure [0.15 eV per formula unit (f.u.)], meaning that, while it is not close to the experimental structure in a sense, it is a lower energy local minimum.

To allow GO-MHALP to find the true global minimum, we prepared three input structures with the same cell type as the experimental structure by first removing the one redundant inorganic layer from the $\sqrt{2} \times \sqrt{2}$ cell type, followed by an extension to a $2\sqrt{2} \times \sqrt{2}$ supercell. We considered three 4AMP configurations: nonalternating, where all 4AMP molecules connect to the perovskite layer in the same manner; alternating, where the 4AMP molecules alternate the manner of connection to the perovskite layer along the long cell axis; and experimental-like, where the manner of connection of the 4AMP molecules to the perovskite layer is alternated for every *second* neighbor. The results of the GO-MHALP run with these structure types are shown in Fig. 10. The global minimum of the potential (the experimental structure relaxed with the classical potential) is found exclusively for the experimental-like connection pattern. Relaxing the initial guess structure of the experimental cell type with DFT achieves a similarity of 0.74, while relaxing the found global minimum achieves a remarkable similarity of 0.968, almost perfectly overlapping the similarity of the experimental structure relaxed with DFT.

D. *t*-$BA_2PbBr_2I_2$

We have employed GO-MHALP to predict a previously unknown Q2DP structure and verified its prediction by single-crystal XRD measurements. We used *tert*-butylammonium (*t*-BA) as the organic spacer. While this is detailed in a separate work [24], we here deepen the discussion of the application of GO-MHALP to that challenging case. The optical measurements indicated that synthesis starting from a one-to-one iodide-bromide stoichiometry results in *t*-$BA_2PbBr_2I_2$, a crystallized $n = 1$ RP phase, while syntheses starting from pure bromide or pure iodide stoichiometries do not yield Q2DP structures [24]. We confirmed the instability of the pure-halide Q2DPs by calculating the formation energies of the global minima found with GO-MHALP as well as by XRD measurements.

To predict the structure of the mixed-halide *t*-$BA_2PbBr_2I_2$, we prepared three types of input structures for GO-MHALP as shown in Fig. 11 with the corresponding GO-MHALP runs shown in Fig. S12 [27]. We see that the minimum corresponding to the experimental structure relaxed with the classical potential is found exclusively starting from the equatorial (axial) bromide (iodine) initial configuration, consistent with the specific halide distribution we found in the structure we resolved experimentally with single-crystal XRD. Relaxing the global minimum with DFT results in a remarkable similarity of 0.967. The relaxed global minimum structure is a local DFT minimum almost isoenergetic to the experimental structure relaxed with DFT (its energy as calculated with DFT is higher by ≈4 meV/f.u.), but it is closer to the experimental structure by ≈0.02 similarity points.

IV. CONCLUSION

In this work, we have introduced a workflow for automatic crystal structure prediction of Q2DP structures. To achieve this, we have developed an automatized initial structure guess and classical potential generation and combined them with a variant of the minima hopping algorithm dubbed GO-MHALP. We tested GO-MHALP on well-known Q2DP structures: BA_2PbBr_4, $BA_2MAPb_2Br_7$, and (4AMP)$PbBr_4$. We have shown that the global minimum is reliably found by GO-MHALP with a weak dependence on the input structure.

The case of (4AMP)$PbBr_4$ suggests that it is necessary to start from a structure with the minimum necessary number of degrees of freedom. We have also shown how GO-MHALP can be used to predict the structure of a mixed-halide Q2DP:

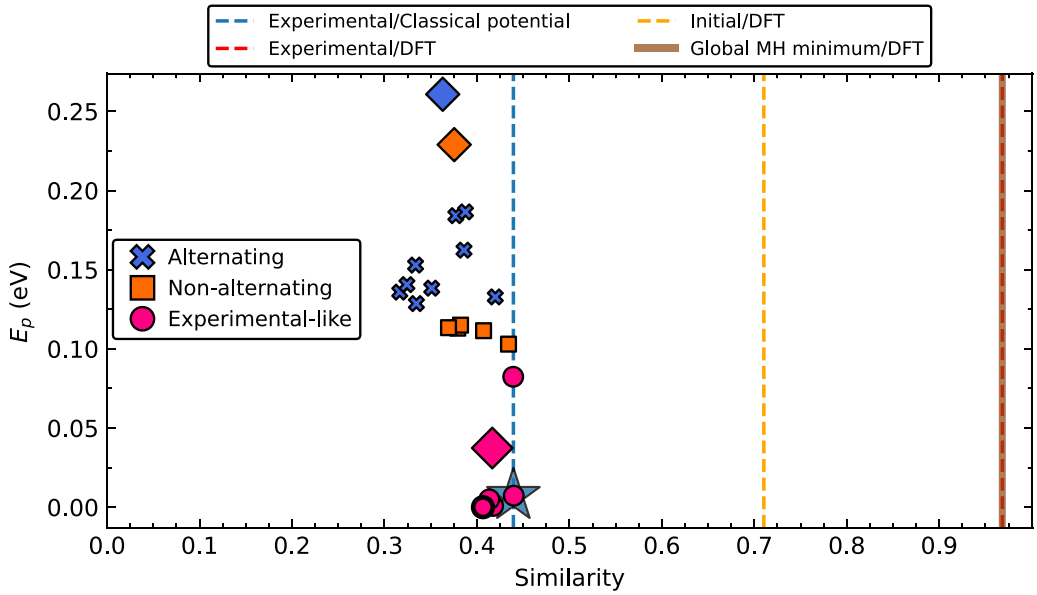

FIG. 10. Similarity measures and (classical) potential energies of (4AMP)$PbBr_4$ starting from the experimental-like $2\sqrt{2} \times \sqrt{2}$ cell type. The vertical dashed lines indicated as X/Y show similarity measures of structures X relaxed with Y level of theory (see text). Different markers indicate different patterns of connection of 4AMP molecules to the inorganic perovskite layer (see text). Diamonds (♦) indicate the starting GO-MHALP points after initial relaxation. The star (★) indicates the similarity measure and energy of the experimental structure relaxed with the classical potential. Energies are shown per formula unit with the zero of the potential energy chosen as the energy of the global GO-MHALP minimum.

t-$BA_2PbBr_2I_2$. We confirmed that not only was the specific halide distribution correctly predicted by GO-MHALP, but also that the structural details were predicted very precisely [24].

While the accuracy of the classical potential itself can be significantly improved, within our method it is not necessary for it to be extremely precise. We have shown that the sufficient condition for a very accurate prediction is only that the global minimum of the potential is connected to the DFT global minimum by a DFT local relaxation. However, the potential should be improved in general to provide reliable predictions for any Q2DP.

We also note that our approach provides physically realistic predictions at a low computational price. Assuming one evaluation of energy and forces with a classical potential is 10^6 times faster than a single self-consistent field (SCF) calculation, 200 GO-MHALP cycles of 25 ps *NPT* simulations take about as long as 5 SCF calculations. This is much less than the number of SCF calculations performed in a typical DFT structural relaxation. Therefore, an unbiased structure prediction may be obtained in less time than necessary for two DFT structural relaxations. Since this computational cost is negligible, GO-MHALP may be further improved by using DFT to relax a larger number of predicted structures around the found global minimum.

Compared to previously available minima hopping algorithms, we implemented several improvements: (i) the MD temperature is restarted after a structurally unique minimum is found; (ii) the replacement scheme, which in combination with (i) ensures detailed exploration of local PES basins; (iii) employment of an *NPT* ensemble for the MD part of minima hopping; and (iv) inclusion of both cell and atomic coordinate relaxations. We believe that these improvements could be employed in structure prediction problems generally whenever multiple kinds of degrees of freedom (configurational, conformational, combinatorial,

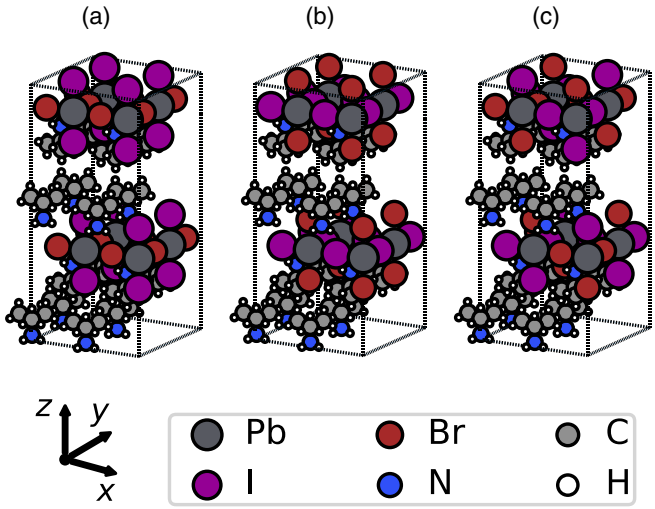

FIG. 11. Starting GO-MHALP structures for *t*-$BA_2PbBr_2I_2$. The cell type is 2×2. The vectors from the nitrogen atoms of the *t*-BA molecules towards the respective centers of mass are aligned with the z axis. The structures differ in the halide distribution, with the bromides (iodides) occupying (a) equatorial (axial), (b) axial (equatorial), and (c) alternating positions.

etc.) render the exploration of PESs particularly difficult, e.g., in soft matter and molecular crystals.

The complete code for generating initial structures, corresponding model potentials, and running GO-MHALP is available free of charge [26]. Using this code all presented data can be regenerated. Derived data are also available from the corresponding author upon reasonable request.

ACKNOWLEDGMENTS

This work was supported by the PZS-2019-02-2068 project financed by the "Research Cooperability" Program of the Croatian Science Foundation and European Union from the European Social Fund under the Operational Programme Efficient Human Resources 2014-2020 and National Natural Science Foundation of China Project No. 6207032617.

[1] A. K. Jena, A. Kulkarni, and T. Miyasaka, Halide perovskite photovoltaics: Background, status, and future prospects, Chem. Rev. **119**, 3036 (2019).

[2] M. Lu, Y. Zhang, S. Wang, J. Guo, W. W. Yu, and A. L. Rogach, Metal halide perovskite light-emitting devices: Promising technology for next-generation displays, Adv. Funct. Mater. **29**, 1902008 (2019).

[3] L. Mao, C. C. Stoumpos, and M. G. Kanatzidis, Two-dimensional hybrid halide perovskites: Principles and promises, J. Am. Chem. Soc. **141**, 1171 (2019).

[4] Z. Chen, Y. Guo, E. Wertz, and J. Shi, Merits and challenges of Ruddlesden-Popper soft halide perovskites in electro-optics and optoelectronics, Adv. Mater. **31**, 1803514 (2019).

[5] S. Ahmad, P. Fu, S. Yu, Q. Yang, X. Liu, X. Wang, X. Wang, X. Guo, and C. Li, Dion-Jacobson phase 2D layered perovskites for solar cells with ultrahigh stability, Joule **3**, 794 (2019).

[6] *Structure Determination from Powder Diffraction Data*, Vol. 13, edited by W. I. F. David, K. Shankland, L. B. McCusker, and C. Bärlocher (Oxford University Press on Demand, Oxford, 2002).

[7] V. Favre-Nicolin and R. Černý, FOX 'free objects for crystallography': A modular approach to *ab initio* structure determination from powder diffraction, J. Appl. Crystallogr. **35**, 734 (2002).

[8] W. I. David, K. Shankland, J. Van De Streek, E. Pidcock, W. S. Motherwell, and J. C. Cole, DASH: A program for crystal structure determination from powder diffraction data, J. Appl. Crystallogr. **39**, 910 (2006).

[9] A. Altomare, C. Cuocci, C. Giacovazzo, A. Moliterni, R. Rizzi, N. Corriero, and A. Falcicchio, Expo2013: A kit of tools for phasing crystal structures from powder data, J. Appl. Crystallogr. **46**, 1231 (2013).

[10] R. Černý, Crystal structures from powder diffraction: Principles, difficulties and progress, Crystals **2017**, 142 (2017).

[11] A. O. Jones, C. Röthel, R. Lassnig, O. Bedoya-Martínez, P. Christian, I. Salzmann, B. Kunert, A. Winkler, and R. Resel, Solution of an elusive pigment crystal structure from a thin film: A combined X-ray diffraction and computational study, CrystEngComm **19**, 1902 (2017).

[12] A. O. Jones, B. Chattopadhyay, Y. H. Geerts, and R. Resel, Substrate-induced and thin-film phases: Polymorphism of organic materials on surfaces, Adv. Funct. Mater. **26**, 2233 (2016).

[13] Q. Tao, P. Xu, M. Li, and W. Lu, Machine learning for perovskite materials design and discovery, npj Comput. Mater. **7**, 23 (2021).

[14] L. Li, Q. Tao, P. Xu, X. Yang, W. Lu, and M. Li, Studies on the regularity of perovskite formation via machine learning, Comput. Mater. Sci. **199**, 110712 (2021).

[15] J. Gómez-Peralta and X. Bokhimi, Ternary halide perovskites for possible optoelectronic applications revealed by artificial intelligence and DFT calculations, Mater. Chem. Phys. **267**, 124710 (2021).

[16] F. Jahanbakhshi, M. Mladenović, M. Dankl, A. Boziki, P. Ahlawat, and U. Rothlisberger, Organic spacers in 2D perovskites: General trends and structure-property relationships from computational studies, Helv. Chim. Acta **104**, e2000232 (2021).

[17] R. Lyu, C. E. Moore, T. Liu, Y. Yu, and Y. Wu, Predictive design model for low-dimensional organic-inorganic halide perovskites assisted by machine learning, J. Am. Chem. Soc. **143**, 12766 (2021).

[18] C. C. Price, J.-C. Blancon, A. D. Mohite, and V. B. Shenoy, Interfacial electromechanics predicts phase behavior of 2D hybrid halide perovskites, ACS Nano **14**, 3353 (2020).

[19] S. Goedecker, Minima hopping: An efficient search method for the global minimum of the potential energy surface of complex molecular systems, J. Chem. Phys. **120**, 9911 (2004).

[20] M. Amsler and S. Goedecker, Crystal structure prediction using the minima hopping method, J. Chem. Phys. **133**, 224104 (2010).

[21] A. A. Peterson, Global optimization of adsorbate-surface structures while preserving molecular identity, Top. Catal. **57**, 40 (2014).

[22] Y. Wang, J. Lv, L. Zhu, and Y. Ma, Calypso: A method for crystal structure prediction, Comput. Phys. Commun. **183**, 2063 (2012).

[23] C. W. Glass, A. R. Oganov, and N. Hansen, USPEX—evolutionary crystal structure prediction, Comput. Phys. Commun. **175**, 713 (2006).

[24] J. Ovčar, T. Leung, L. Grisanti, v. Skoko, M. Vrankić, K.-H. Low, S. Wang, P.-Y. You, H. Ahn, I. Lončarić, A. Djurišić, and J. Popović, Mixed halide ordering as a tool for the stabilization of Ruddlesden-Popper structures, Chem. Mater. **34**, 4286 (2022).

[25] X. Li, J. M. Hoffman, and M. G. Kanatzidis, The 2D halide perovskite rulebook: How the spacer influences everything from the structure to optoelectronic device efficiency, Chem. Rev. **121**, 2230 (2021).

[26] https://github.com/ovcarj/classical-RPP/tree/ase2020

[27] See Supplemental Material at http://link.aps.org/supplemental/10.1103/PhysRevB.107.174109 for details on initial structure generation, benchmarking the classical potentials against DFT, detailed structural analysis of relevant structures. The initial and the most relevant found structures are given in CIF format. The Supplemental Material also contains Refs. [32,77–79].

[28] M. Matsui, M. Akaogi, and T. Matsumoto, Computational model of the structural and elastic properties of the ilmenite and perovskite phases of $MgSiO_3$, Phys. Chem. Miner. **14**, 101 (1987).

[29] M. I. Saba and A. Mattoni, Effect of thermodynamics and curvature on the crystallinity of P3HT thin films on ZnO: Insights from atomistic simulations, J. Phys. Chem. C **118**, 4687 (2014).

[30] A. Mattoni, A. Filippetti, M. Saba, and P. Delugas, Methylammonium rotational dynamics in lead halide perovskite by classical molecular dynamics: The role of temperature, J. Phys. Chem. C **119**, 17421 (2015).

[31] T. Hata, G. Giorgi, K. Yamashita, C. Caddeo, and A. Mattoni, Development of a classical interatomic potential for $MAPbBr_3$, J. Phys. Chem. C **121**, 3724 (2017).

[32] M. B. Fridriksson, N. Van Der Meer, J. De Haas, and F. C. Grozema, Tuning the structural rigidity of two-dimensional Ruddlesden-Popper perovskites through the organic cation, J. Phys. Chem. C **124**, 28201 (2020).

[33] J. Wang, R. M. Wolf, J. W. Caldwell, P. A. Kollman, and D. A. Case, Development and testing of a general Amber force field, J. Comput. Chem. **25**, 1157 (2004).

[34] J. W. Ponder and D. A. Case, Force fields for protein simulations, in *Advances in Protein Chemistry*, Vol. 66 (Elsevier, Amsterdam, 2003), pp. 27–85.

[35] D. Marx and J. Hutter, *Ab Initio Molecular Dynamics: Basic Theory and Advanced Methods* (Cambridge University Press, Cambridge, U.K., 2009).

[36] R. A. Buckingham, The classical equation of state of gaseous helium, neon and argon, Proc. R. Soc. London A **168**, 264 (1938).

[37] D. Weber, $CH_3NH_3PbX_3$, ein Pb(II)-system mit kubischer perowskitstruktur/$CH_3NH_3PbX_3$, a Pb(II)-system with cubic perovskite structure, Z. Naturforsch. B **33**, 1443 (1978).

[38] T. Zhu and E. Ertekin, Mixed phononic and non-phononic transport in hybrid lead halide perovskites: Glass-crystal duality, dynamical disorder, and anharmonicity, Energy Environ. Sci. **12**, 216 (2019).

[39] M. Wuttig, C.-F. Schön, M. Schumacher, J. Robertson, P. Golub, E. Bousquet, C. Gatti, and J.-Y. Raty, Halide perovskites: Advanced photovoltaic materials empowered by a unique bonding mechanism, Adv. Funct. Mater. **32**, 2110166 (2022).

[40] A. Mattoni, A. Filippetti, and C. Caddeo, Modeling hybrid perovskites by molecular dynamics, J. Phys.: Condens. Matter **29**, 043001 (2017).

[41] R. W. Hockney and J. W. Eastwood, *Computer Simulation Using Particles* (CRC Press, Boca Raton, FL, 1988).

[42] M. J. Frisch, G. W. Trucks, H. B. Schlegel, G. E. Scuseria, M. A. Robb, J. R. Cheeseman, G. Scalmani, V. Barone, G. A. Petersson, H. Nakatsuji, X. Li, M. Caricato, A. Marenich, J. Bloino, B. G. Janesko, R. Gomperts, B. Mennucci, H. P. Hratchian, J. V. Ortiz, A. F. Izmaylov *et al.*, *Gaussian 09 Revision D.01* (Gaussian Inc., Wallingford, CT, 2016).

[43] A. D. Becke, Density-functional exchange-energy approximation with correct asymptotic behavior, Phys. Rev. A **38**, 3098 (1988).

[44] C. Lee, W. Yang, and R. G. Parr, Development of the Colle-Salvetti correlation-energy formula into a functional of the electron density, Phys. Rev. B **37**, 785 (1988).

[45] S. H. Vosko, L. Wilk, and M. Nusair, Accurate spin-dependent electron liquid correlation energies for local spin density calculations: A critical analysis, Can. J. Phys. **58**, 1200 (1980).

[46] P. J. Stephens, F. J. Devlin, C. F. Chabalowski, and M. J. Frisch, Ab initio calculation of vibrational absorption and circular dichroism spectra using density functional force fields, J. Phys. Chem. **98**, 11623 (1994).

[47] A. McLean and G. Chandler, Contracted Gaussian basis sets for molecular calculations. I. Second row atoms, $z = 11$–18, J. Chem. Phys. **72**, 5639 (1980).

[48] T. Clark, J. Chandrasekhar, G. W. Spitznagel, and P. V. R. Schleyer, Efficient diffuse function-augmented basis sets for anion calculations. III. The 3-21+G basis set for first-row elements, Li–F, J. Comput. Chem. **4**, 294 (1983).

[49] R. Krishnan, J. S. Binkley, R. Seeger, and J. A. Pople, Self-consistent molecular orbital methods. XX. A basis set for correlated wave functions, J. Chem. Phys. **72**, 650 (1980).

[50] A. D. Becke, Density-functional thermochemistry. III. The role of exact exchange, J. Chem. Phys. **98**, 5648 (1993).

[51] J. P. Perdew and Y. Wang, Accurate and simple density functional for the electronic exchange energy: Generalized gradient approximation, Phys. Rev. B **33**, 8800 (1986).

[52] J. P. Perdew and Y. Wang, Accurate and simple analytic representation of the electron-gas correlation energy, Phys. Rev. B **45**, 13244 (1992).

[53] F. Weigend and R. Ahlrichs, Balanced basis sets of split valence, triple zeta valence and quadruple zeta valence quality for H to Rn: Design and assessment of accuracy, Phys. Chem. Chem. Phys. **7**, 3297 (2005).

[54] F. Weigend, Accurate Coulomb-fitting basis sets for H to Rn, Phys. Chem. Chem. Phys. **8**, 1057 (2006).

[55] C. I. Bayly, P. Cieplak, W. Cornell, and P. A. Kollman, A well-behaved electrostatic potential based method using charge restraints for deriving atomic charges: The RESP model, J. Phys. Chem. **97**, 10269 (1993).

[56] J. Wang, W. Wang, P. A. Kollman, and D. A. Case, Automatic atom type and bond type perception in molecular mechanical calculations, J. Mol. Graphics Modell. **25**, 247 (2006).

[57] D. A. Case, H. M. Aktulga, K. Belfon, I. Y. Ben-Shalom, J. T. Berryman, S. R. Brozell, D. S. Cerutti, T. E. Cheatham, III, G. A. Cisneros, V. W. D. Cruzeiro, T. A. Darden, N. Forouzesh, G. Giambau, T. Giese, M. K. Gilson, H. Gohlke, A. W. Goetz, J. Harris, S. Izadi, S. A. Izmailov, K. Kasavajhala, M. C. Kaymak, E. King, A. Kovalenko, T. Kurtzman, T. S. Lee, P. Li, C. Lin, J. Liu, T. Luchko, R. Luo, M. Machado, V. Man, M. Manathunga, K. M. Merz, Y. Miao, O. Mikhailovskii, G. Monard, H. Nguyen, K. A. O'Hearn, A. Onufriev, F. Pan, S. Pantano, R. Qi, A. Rahnamoun, D. R. Roe, A. Roitberg, C. Sagui, S. Schott-Verdugo, A. Shajan, J. Shen, C. L. Simmerling, N. R. Skrynnikov, J. Smith, J. Swails, R. C. Walker, J. Wang, J. Wang, H. Wei, X. Wu, Y. Wu, Y. Xiong, Y. Xue, D. M. York, S. Zhao, Q. Zhu, and P. A. Kollman, *Amber 2023* (University of California, San Francisco, 2023).

[58] R. Salomon-Ferrer, D. A. Case, and R. C. Walker, An overview of the Amber biomolecular simulation package, Wiley Interdisc. Rev.: Comput. Mol. Sci. **3**, 198 (2013).

[59] S. Plimpton, Fast parallel algorithms for short-range molecular dynamics, J. Comput. Phys. **117**, 1 (1995).

[60] A. H. Larsen, J. J. Mortensen, J. Blomqvist, I. E. Castelli, R. Christensen, M. Dułak, J. Friis, M. N. Groves, B. Hammer, C. Hargus *et al.*, The atomic simulation environment—a PYTHON library for working with atoms, J. Phys.: Condens. Matter **29**, 273002 (2017).

[61] S. Melchionna, G. Ciccotti, and B. Lee Holian, Hoover NPT dynamics for systems varying in shape and size, Mol. Phys. **78**, 533 (1993).

[62] S. Melchionna, Constrained systems and statistical distribution, Phys. Rev. E **61**, 6165 (2000).

[63] B. L. Holian, A. J. De Groot, W. G. Hoover, and C. G. Hoover, Time-reversible equilibrium and nonequilibrium isothermal-isobaric simulations with centered-difference Stoermer algorithms, Phys. Rev. A **41**, 4552 (1990).

[64] A. R. Oganov and M. Valle, How to quantify energy landscapes of solids, J. Chem. Phys. **130**, 104504 (2009).

[65] A. O. Lyakhov, A. R. Oganov, and M. Valle, How to predict very large and complex crystal structures, Comput. Phys. Commun. **181**, 1623 (2010).

[66] P. Giannozzi, S. Baroni, N. Bonini, M. Calandra, R. Car, C. Cavazzoni, D. Ceresoli, G. L. Chiarotti, M. Cococcioni, I. Dabo *et al.*, QUANTUM ESPRESSO: A modular and open-source software project for quantum simulations of materials, J. Phys.: Condens. Matter **21**, 395502 (2009).

[67] P. Giannozzi, O. Andreussi, T. Brumme, O. Bunau, M. B. Nardelli, M. Calandra, R. Car, C. Cavazzoni, D. Ceresoli, M. Cococcioni *et al.*, Advanced capabilities for materials modelling with QUANTUM ESPRESSO, J. Phys.: Condens. Matter **29**, 465901 (2017).

[68] K. F. Garrity, J. W. Bennett, K. M. Rabe, and D. Vanderbilt, Pseudopotentials for high-throughput DFT calculations, Comput. Mater. Sci. **81**, 446 (2014).

[69] K. Berland, C. A. Arter, V. R. Cooper, K. Lee, B. I. Lundqvist, E. Schroder, T. Thonhauser, and P. Hyldgaard, Van der Waals density functionals built upon the electron-gas tradition: Facing the challenge of competing interactions, J. Chem. Phys. **140**, 18A539 (2014).

[70] H. J. Monkhorst and J. D. Pack, Special points for Brillouin-zone integrations, Phys. Rev. B **13**, 5188 (1976).

[71] R. de Gelder, R. Wehrens, and J. A. Hageman, A generalized expression for the similarity of spectra: Application to powder diffraction pattern classification, J. Comput. Chem. **22**, 273 (2001).

[72] S. Habermehl, P. Mörschel, P. Eisenbrandt, S. M. Hammer, and M. U. Schmidt, Structure determination from powder data without prior indexing, using a similarity measure based on cross-correlation functions, Acta. Crystallogr. B Struct. Sci. Cryst. Eng. Mater. **70**, 347 (2014).

[73] S. Fredericks, K. Parrish, D. Sayre, and Q. Zhu, Pyxtal: A PYTHON library for crystal structure generation and symmetry analysis, Comput. Phys. Commun. **261**, 107810 (2021).

[74] X. Gong, O. Voznyy, A. Jain, W. Liu, R. Sabatini, Z. Piontkowski, G. Walters, G. Bappi, S. Nokhrin, O. Bushuyev *et al.*, Electron-phonon interaction in efficient perovskite blue emitters, Nat. Mater. **17**, 550 (2018).

[75] L. Li, X. Liu, Y. Li, Z. Xu, Z. Wu, S. Han, K. Tao, M. Hong, J. Luo, and Z. Sun, Two-dimensional hybrid perovskite-type ferroelectric for highly polarization-sensitive shortwave photodetection, J. Am. Chem. Soc. **141**, 2623 (2019).

[76] L. Mao, W. Ke, L. Pedesseau, Y. Wu, C. Katan, J. Even, M. R. Wasielewski, C. C. Stoumpos, and M. G. Kanatzidis, Hybrid Dion-Jacobson 2D lead iodide perovskites, J. Am. Chem. Soc. **140**, 3775 (2018).

[77] N. Michaud-Agrawal, E. J. Denning, T. B. Woolf, and O. Beckstein, MDAnalysis: A toolkit for the analysis of molecular dynamics simulations, J. Comput. Chem. **32**, 2319 (2011).

[78] R. J. Gowers, M. Linke, J. Barnoud, T. J. Reddy, M. N. Melo, S. L. Seyler, J. Domanski, D. L. Dotson, S. Buchoux, I. M. Kenney *et al.*, MDAnalysis: A PYTHON package for the rapid analysis of molecular dynamics simulations, in *Proceedings of the 15th Python in Science Conference*, Vol. 98 (SciPy, Austin, TX, 2016), p. 105.

[79] K.-z. Du, Q. Tu, X. Zhang, Q. Han, J. Liu, S. Zauscher, and D. B. Mitzi, Two-dimensional lead(II) halide-based hybrid perovskites templated by acene alkylamines: Crystal structures, optical properties, and piezoelectricity, Inorg. Chem. **56**, 9291 (2017).